Evolution of a Potential Vorticity Front over a Topographic Slope

R. GRIMSHAW

School of Mathematics, University of New South Wales, Kensington, New South Wales, Australia

ZENGXIN YI

National Research Center for Marine Environment Forecasts, State Oceanic Administration, Beijing, China

(Manuscript received 22 October 1990, in final form 5 March 1991)

ABSTRACT

Using the methodology of contour dynamics, the evolution of an interface separating two regions of constant potential vorticity is considered. The model equations are those for barotropic nondivergent flow over a topographic slope adjoined by a coastal barrier. The main focus is on the processes which lead to wave breaking for small-amplitude waves and, in general agreement with previous related work, it is found that wave steepening leads to the formation of thin filaments. The key parameter is found to be the ratio of the background potential vorticity to the discontinuity of potential vorticity across the front, with other parameters such as the topographic slope and the distance to the coast playing a relatively less significant role.

1. Introduction

Coastal currents are often characterized by meanders and squirts, which sometimes lead to the formation of detached eddies. These features are usually of a sufficient amplitude to require a nonlinear theory for their theoretical description. In a previous paper Grimshaw and Yi (1990) developed some models for the description of finite-amplitude long waves on coastal currents. However, although that approach was successful in identifying various families of waves, the long-wave hypothesis precludes a study of wave evolution that incorporates all length-scales. This is particularly pertinent when the long waves are observed to be steepening. Hence, in the present paper, we seek to remedy this defect by using the methodology of contour dynamics to extend one of the models developed by Grimshaw and Yi (1990) to all length scales. This model describes the waves that form at a vorticity interface separating two regions of constant potential vorticity, and is typical of the configurations that are amenable to the techniques of contour dynamics.

Although contour dynamics is barely a decade old, it has developed rapidly both with respect to the sophistication of the algorithms and with respect to the range of applications, and is now established as a powerful method for studying two-dimensional inviscid fluid flows (see, for instance, the recent review by Dritschel 1989). Of the many oceanographic applications, that which is closest to the present work is the study by Pratt and Stern (1986) on the evolution of a vorticity front separating two regions of constant potential vorticity in a $1\frac{1}{2}$-layer quasi-geostrophic model. Here, a vorticity front separating two regions of constant potential vorticity is also considered, but in the context of a nondivergent barotropic model for flow on the continental shelf and slope. The essential difference is the presence of the topographic slope, which in the present paper is retained in full; that is, we do not make the quasi-geostrophic approximation of a weak slope. However, in order to obtain a relatively simple contour dynamic algorithm we eventually assume that the vorticity front lies entirely over the topographic slope and well away from the shelf-break where the continental slope adjoins the ocean whose topographic slope is zero. The important question of how a vorticity front might behave at the shelf-break is left for a later study, while here we concentrate on the role of the coastal boundary and topographic slope on the evolution of a vorticity front. In developing a contour dynamics algorithm for the present application, the most sophisticated routines currently available for node insertion and deletion are not used, since our main aim is the study of wave evolution and the processes leading to filamentation, rather than the details of filamentation itself. Hence we are able to obtain computational simplicity and efficiency while retaining sufficient resolution to determine how waves on a vorticity interface evolve and possibly develop filaments. After completion of our work we became aware of the paper by Send (1989), which treats a similar problem on the behavior of potential vorticity

Corresponding author address: Dr. Roger Grimshaw, School of Mathematics, University of New South Wales, P.O. Box 1, Kensington, New South Wales 2033, Australia

fronts over topographic slopes. The essential difference between Send's and our work is that Send considers wave evolution on an unstable basic flow which requires the use of two or three contours, whereas we consider only waves on a stable basic flow using just one contour. Further we give a detailed investigation of the parameter regime whereas Send considers only parameters appropriate to models of the California Current system. There are also some differences in formulation which are mentioned later in the appropriate place.

In section 2 the equations of motion for barotropic nondivergent flow over a topographic slope are formulated. Then, assuming that the flow can be described by the evolution of a potential vorticity interface separating two regions of constant potential vorticity (see Fig. 1), the equations are recast into a format suitable for the development of a contour dynamics algorithm. In this section the topographic slope is not specified precisely in order to demonstrate that the contour dynamics algorithm can in principle be formulated for quite general topographic slopes. However, it should be pointed out that the wave restoring mechanism in this model is not due directly to the topographic slope, but is due to the potential vorticity gradient; that is, it is due to the potential vorticity jump across the interface. The value of this jump is maintained by a combination of the topographic slope and the basic longshore current.

Next, to make analytical and numerical progress, we must choose a specific topographic slope which is the familiar exponential depth profile. This is done in section 3, which is in two parts. In the first we obtain the Green's function needed for inverting the vorticity–streamfunction relation and hence the velocity fields at the vorticity interface. At this stage we also introduce the approximation that the vorticity interface is far removed from the shelf-break. In the second part of section 3, a brief description of the contour dynamics algorithm is given. A reader not concerned with the details of the Green's function and the numerical procedure could proceed directly from section 2 to section 4, where our results are presented. We conclude with a summary in section 5.

2. Formulation

We shall use nondimensional coordinates based on a horizontal length scale L_1 (a typical wavelength), a time scale f_1^{-1} (f_1 is the magnitude of the Coriolis parameter) and a vertical depth scale h_1 (a typical depth). The equations of motion for barotropic nondivergent flow are then

$$\frac{du}{dt} - fv + p_x = 0, \tag{2.1a}$$

$$\frac{dv}{dt} + fu + p_y = 0, \tag{2.1b}$$

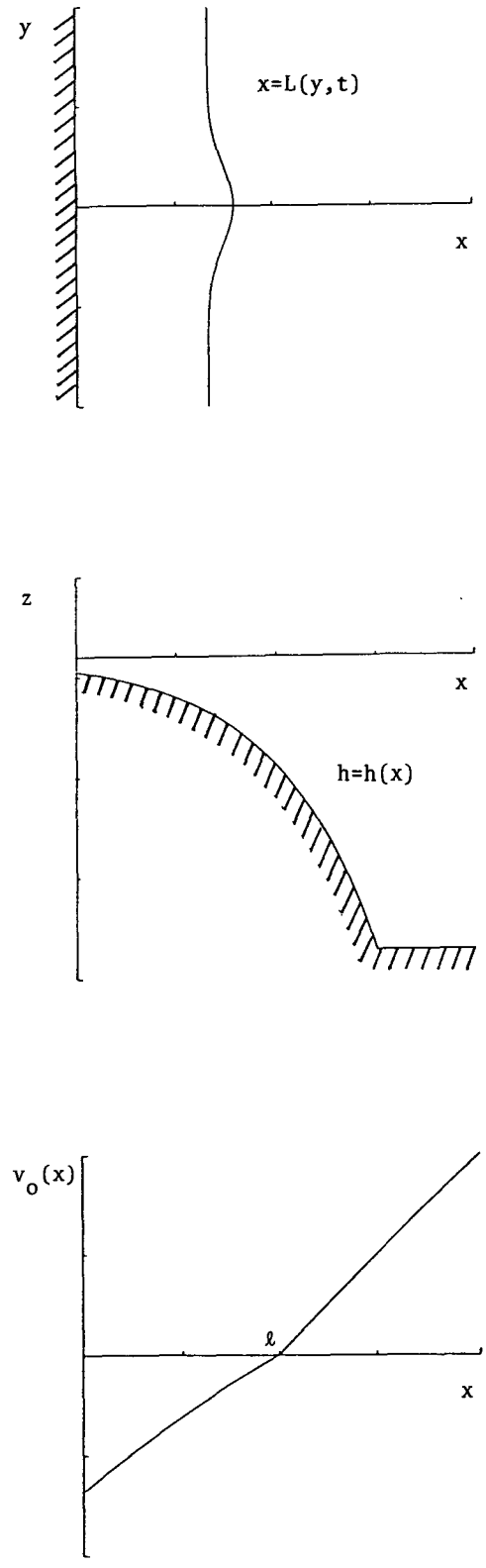

FIG. 1. The coordinate system and definition sketches. (a) Plan view of the potential vorticity interface; (b) the exponential depth profile; (c) the basic longshore current (3.15). For (b), (c) the parameter setting is $s = 1$, $\gamma_1 = 2$, $l = 1$ and $\Delta Q h_1 = -1$.

$$(hu)_x + (hv)_y = 0, \tag{2.1c}$$

where

$$\frac{d}{dt} = \frac{\partial}{\partial t} + u\frac{\partial}{\partial x} + v\frac{\partial}{\partial y}. \tag{2.1d}$$

Here u, v are the velocity components in the x, y directions, respectively, and p is the sea-surface elevation. The coast is located at $x = 0$ and the ocean depth is $h(x)$ where $h(x)$ is an increasing function of x which tends to h_0 as $x \to \infty$. Elimination of p from (2.1a, b) leads to the potential vorticity equation

$$\frac{dq}{dt} = 0, \tag{2.2a}$$

where

$$q = \frac{f + \zeta}{h}, \tag{2.2b}$$

and

$$\zeta = v_x - u_y. \tag{2.2c}$$

Next (2.1c) is used to introduce the transport stream function ψ, such that

$$hu = \psi_y, \quad hv = -\psi_x. \tag{2.3}$$

Hence, from (2.2b, c)

$$hq = f - \left(\frac{\psi_x}{h}\right)_x - \frac{\psi_{yy}}{h}, \tag{2.4}$$

and (2.2a) is an equation for ψ alone. The boundary conditions are that

$$\psi = 0, \quad \text{at} \quad x = 0, \tag{2.5a}$$

and

$$\psi_y \to 0, \quad \text{as} \quad x \to \infty, \tag{2.5b}$$

which are the conditions for zero flux in the on–offshore direction at the coast and in the distant ocean, respectively.

We wish to consider the waves which form on the interface separating two regions of constant potential vorticity. As discussed in the Introduction, the basic methodology is that of contour dynamics, although its implementation is complicated here by the bottom topography. Thus, we let $x = L(y, t)$ denote the interface between two regions of constant potential vorticity, where $L > 0$ and $L \to l$ as $y \to -\infty$ (see Fig. 1.). Hence

$$q = Q_1, \quad \text{for} \quad 0 < x < L, \tag{2.6a}$$

$$q = Q_0, \quad \text{for} \quad x > L. \tag{2.6b}$$

Since it is anticipated that the interface will develop folds and filaments we shall allow $x = L(y, t)$ to be a multivalued function of y, and denote the interface simply by $\mathcal{C}$, although it is convenient nevertheless to retain the $x = L(y, t)$ formulation in developing the theory. The boundary conditions on $\mathcal{C}$ are the kinematic condition

$$L_t + vL_y = u, \tag{2.7}$$

and the continuity of the tangential velocity (Grimshaw and Yi 1990), where it is noted that (2.7) implies the continuity of the normal velocity. For the purposes of contour dynamics it is convenient to replace these boundary conditions with the equivalent Lagrangian conditions that each Lagrangian point (L, y) on $\mathcal{C}$ is moved according to the prescription

$$\frac{dL}{dt} = u(L, y, t), \quad \frac{dy}{dt} = v(L, y, t). \tag{2.8}$$

Next we examine the structure of the basic longshore current $v_0(x)$ which supports the piecewise constant potential vorticity distribution in the limit $y \to -\infty$, where $L \to l$ and $u \to 0$. Hence from (2.2b, c) and (2.6a, b) it is defined by

$$v_{0x} = \begin{cases} -f + Q_1 h, & \text{for} \quad 0 < x < l \\ -f + Q_0 h, & \text{for} \quad x > l. \end{cases} \tag{2.9}$$

With $v_0(x)$ continuous at $x = l$, we find that

$$v_0(x) = V + (Q_0 h_0 - f)(x - l) + Q_0 \int_l^x \{h(x') - h_0\} dx' + (Q_1 - Q_0) H(l - x) \int_l^x h(x') dx'. \tag{2.10}$$

We now require that v_0 is finite as $x \to \infty$ so that $Q_0 = f/h_0$, and for convenience put the constant of integration $V = 0$ so that $v_0(l) = 0$. Here $H(\cdot)$ is the Heaviside function, and we recall that $h \to h_0$ as $x \to \infty$. The corresponding basic streamfunction $\psi_0(x)$ is given by

$$\psi_0(x) = -\int_0^x v_0(x') h(x') dx'. \tag{2.11}$$

A definition sketch of $v_0(x)$ is given in Fig. 1 for the case when the topographic slope is given by the exponential depth profile $h = h_1 \exp[s(x - l)]$ for $0 < x < x_0$ and is a constant for $x > x_0$ [see (3.3a, b)]; in this case $v_0(x)$ can be evaluated explicitly from (2.10) and is given by (3.15).

Next, we put

$$\psi = \psi_0(x) + \phi, \tag{2.12}$$

and substitute this expression into (2.4) and (2.6a, b) to get

$$\left(\frac{\phi_x}{h}\right)_x + \frac{\phi_{yy}}{h} = \begin{cases} -\Delta Q h, & \text{for} \quad l < x < L \\ \Delta Q h, & \text{for} \quad L < x < l \\ 0, & \text{otherwise} \end{cases} \tag{2.13a}$$

where

$$\Delta Q = Q_1 - Q_0. \tag{2.13b}$$

The boundary conditions are that

$$\phi = 0, \quad \text{at} \quad x = 0, \tag{2.14a}$$

$$\phi \to 0 \quad \text{as} \quad x^2 + y^2 \to \infty, \tag{2.14b}$$

and ϕ, ϕ_x, ϕ_y are continuous across $\mathscr{C}$. To solve (2.13a) we introduce the Green's function $G(x, \xi; y - \eta)$, which is defined by

$$\left(\frac{G_x}{h}\right)_x + \frac{G_{yy}}{h} = \delta(x - \xi)\delta(y - \eta), \tag{2.15a}$$

$$G = 0, \quad \text{at} \quad x = 0, \tag{2.15b}$$

and

$$G \to 0, \quad \text{as} \quad x^2 + y^2 \to \infty. \tag{2.15c}$$

It can now be shown that, using standard manipulations involving Green's integral identities,

$$\phi(x, y, t) = -\Delta Q \int_{-\infty}^{\infty} dy' \times \int_{l}^{L(y',t)} G(x', x; y' - y)h(x')dx'. \tag{2.16}$$

The corresponding velocity fields are obtained from (2.3) and (2.12) so that

$$u(x, y, t) = -\frac{\Delta Q}{h(x)} \int_{-\infty}^{\infty} dy' \times \int_{l}^{L(y',t)} \frac{\partial G}{\partial y}(x', x; y' - y)h(x')dx', \tag{2.17a}$$

and

$$v(x, y, t) - v_0(x) = \frac{\Delta Q}{h(x)} \int_{-\infty}^{\infty} dy' \times \int_{l}^{L(y',t)} \frac{\partial G}{\partial x}(x', x; y' - y)h(x')dx'. \tag{2.17b}$$

Once the Green's function $G(x', x; y' - y)$ has been found from (2.15a–c), the expressions (2.17a, b) combined with (2.8) give a set of integro–differential equations for the evolution of the contour $\mathscr{C}$. This is the essence of the contour dynamics approach. However, to be useful, two further steps are required. The first step is to obtain an analytical expression for the Green's function, which requires a specification of the depth $h(x)$. As indicated previously, the exponential depth profile (3.3a, b) is used. Combined with the approximation that the contour lies entirely over the slope (i.e., L, $l \ll x_0$ where $h = h_0$ is a constant for $x > x_0$), this then leads to a relatively simple explicit formula for the Green's function [see (3.7)]. This calculation is deferred until section 3, but we note here that near the source point

$$G(x', x; y' - y) \approx \frac{h(x)}{2\pi} \log(R/R_I), \quad \text{as} \quad R \to 0, \tag{2.18a}$$

where

$$R = \{(x - x')^2 + (y - y')^2\}^{1/2} \tag{2.18b}$$

and

$$R_I = \{(x + x')^2 + (y - y')^2\}^{1/2}. \tag{2.18c}$$

Note that the image term is included to satisfy the coastal boundary condition (2.15b), and that for a constant depth, (2.18a) is an exact result. Hence we anticipate that it may be useful for weak slopes. The second step is to convert the expressions (2.17a, b) from integrals over the area occupied by the displaced contour to integrals along the contour $\mathscr{C}$ itself. In the case of (2.16a) this is readily accomplished by observing that the Green's function depends only on $y' - y$, converting the y-derivative to a y'-derivative and integrating by parts to get

$$u(x, y, t) = -\frac{\Delta Q}{h(x)} \int_{-\infty}^{\infty} h(L')G(L', x; y' - y)dL', \tag{2.19a}$$

where

$$L' = L(y', t), \tag{2.19b}$$

and

$$dL' = \frac{\partial L}{\partial y'} dy'. \tag{2.19c}$$

However, a similar procedure cannot be immediately applied to (2.17b) until an analytical expression for the Green's function is obtained in section 3.

To conclude this section we reconstruct the long-wave approximation for the evolution of the contour, given by Grimshaw and Yi (1990). This could be obtained by approximating the Green's function but it is simpler to obtain an approximation for $\phi(x, y, t)$ directly. Turning to (2.13a), suppose that $h = h_0$ for $x > x_0$ and that the contour lies entirely in the region $0 < x < x_0$. Then for $x > x_0$ the solution of (2.13a), which satisfies the boundary condition (2.15b), is given by

$$\phi = \frac{1}{2\pi} \int_{\infty}^{\infty} \mathcal{F}(B) \exp[iky - |k|(x - x_0)]dk, \tag{2.20a}$$

where

$$\mathcal{F}(B) = \int_{-\infty}^{\infty} B(y, t) \exp(-iky)dk, \tag{2.20b}$$

and

$$B = \phi(x_0, y, t). \tag{2.20c}$$

Next, for $0 < x < x_0$, the long-wave approximation implies that the y-derivatives in (2.13a) can be neglected. Hence an approximate solution of (2.13a), which satisfies the boundary condition (2.14a) and matches smoothly with the solution (2.20a) at $x = x_0$, is readily constructed. When combined with $\psi_0(x)$ [see (2.11) and (2.12)], we find that

$$\psi(L, y, t) \approx \frac{f}{h_0}\int_0^L h(x)dx \int_l^x [h_0 - h(x')]dx' + \Delta Q\left\{\frac{1}{2}J^2 + \frac{J}{h_0}\mathcal{B}(M)\right\}, \quad (2.21a)$$

where

$$M = \frac{1}{2}(J^2 - j^2) \quad (2.21b)$$

$$J = \int_0^L h(x)dx, \quad j = \int_0^l h(x)dx, \quad (2.21c)$$

and

$$\mathcal{B}(M) = -\frac{1}{2\pi}\int_{-\infty}^{\infty} |k|\mathcal{F}(M)\exp(iky)dk. \quad (2.21d)$$

Now, using (2.3), (2.7) can be put in the form

$$h(L)L_t = \frac{\partial}{\partial y}\{\psi(L, y, t)\}, \quad (2.22)$$

and substituting the approximate expression (2.21a) into (2.22), we obtain an evolution equation for L. After allowing for a different notation, this agrees with the equation discussed by Grimshaw and Yi (1990). They discuss various numerical solutions that show a tendency towards wave steepening. Indeed, as discussed in the Introduction, our main aim in this paper is to relax the long-wave approximation and determine the consequences of wave steepening. In the weakly nonlinear, nondispersive limit, (2.22) reduces to

$$L_t = \Delta Q h_1\{c_0 L_y + [1 + \gamma_1(1 - \delta)](L - l)L_y\} \quad (2.23a)$$

where

$$c_0 = \frac{1}{h_1}\int_0^l h(x)dx, \quad h_1 = h(l), \quad (2.23b)$$

and

$$\gamma_1 = \frac{f}{\Delta Q h_1}, \quad \delta = \frac{h_1}{h_0}. \quad (2.23c)$$

Thus, small-amplitude long waves propagate with speed c_0 in the positive (negative) y-direction if $\Delta Q < 0 (>0)$, and will steepen in the forward (backward) direction if $[1 + \gamma_1(1 - \delta)] > 0 (<0)$.

3. Green's function evaluation and numerical method

a. Green's function evaluation

The Green's function is defined by (2.15a–c). To solve this system in general, we take a Fourier transform in y so that

$$G(x, \xi; y - \eta) = \frac{1}{2\pi}\int_{-\infty}^{\infty} \hat{G}(x, \xi; k)\exp[ik(y - \eta)]dk. \quad (3.1)$$

Then from (2.15a–c) it follows that $\hat{G}$ is obtained from

$$\left(\frac{\hat{G}_x}{h}\right)_x - \frac{k^2\hat{G}}{h} = \delta(x - \xi), \quad (3.2a)$$

$$\hat{G} = 0, \quad \text{at} \quad x = 0, \quad (3.2b)$$

and

$$\hat{G} \to 0, \quad \text{as} \quad x \to \infty. \quad (3.2c)$$

Next we suppose that $h = h_0$ for $x > x_0$, so that

$$\hat{G}(x, \xi; k) = \hat{G}(x_0, \xi; k)\exp[-|k|(x - x_0)], \quad \text{for} \quad x \geq x_0. \quad (3.3)$$

To make further progress, a specific depth profile must be chosen, and we use the exponential depth profile given by

$$h(x) = h_1\exp[s(x - l)] \quad \text{for} \quad 0 < x < x_0, \quad (3.3a)$$

so that

$$h_0 = h_1\exp[s(x_0 - l)]. \quad (3.3b)$$

Note that h_1 is the depth at the undisplaced position of the interface [see (2.23b)]. Then it may be shown that, when $0 < \xi < x_0$,

$$\hat{G} = \frac{\{h(x)h(\xi)\}^{1/2}}{W(k)}\phi_1(x; k)\phi_2(\xi; k), \quad \text{for} \quad 0 \leq x \leq \xi, \quad (3.4a)$$

and

$$\hat{G} = \frac{\{h(x)h(\xi)\}^{1/2}}{W(k)}\phi_1(\xi; k)\phi_2(x; k), \quad \text{for} \quad \xi \leq x \leq x_0, \quad (3.4b)$$

where

$$\phi_1(x; k) = \sinh\left[\left(k^2 + \frac{1}{4}s^2\right)^{1/2}x\right], \quad (3.4c)$$

$$\phi_2(x; k) = \cosh\left[\left(k^2 + \frac{1}{4}s^2\right)^{1/2}(x_0 - x)\right]$$

$$+\frac{\left(|k|+\frac{1}{2}s\right)}{\left(k^2+\frac{1}{4}s^2\right)^{1/2}}\sinh\left[\left(k^2+\frac{1}{4}s^2\right)^{1/2}(x_0-x)\right] \tag{3.4d}$$

and

$$W(k)=-\left(k^2+\tfrac{1}{4}s^2\right)^{1/2}\cosh\left[\left(k^2+\tfrac{1}{4}s^2\right)^{1/2}x_0\right]-\left(|k|+\tfrac{1}{2}s\right)\sinh\left[\left(k^2+\tfrac{1}{4}s^2\right)^{1/2}x_0\right]. \tag{3.4e}$$

However, even though the expressions (3.4a, b) for $\hat{G}$ are explicit, to make further progress in obtaining G it is necessary to introduce some approximations. First, it is noted that if $s=0$, so that $h=h_0$ everywhere, then

$$\phi_1(x;k)=\sinh(|k|x), \tag{3.5c}$$

$$\frac{\phi_2(x;k)}{W(k)}=-\frac{1}{|k|}\exp(-|k|x). \tag{3.5d}$$

Substitution of $\hat{G}$ into (3.1) then readily shows that G is given by (2.18a) as expected, indicating that this may be a useful approximation when $s \ll 1$. However, this approach is not pursued, since we wish to take full account of the topographic slope. Hence, instead we shall use the approximation that the contour lies entirely over the slope at all times (i.e., $0<l, L<x_0$) and that $L, l \ll x_0$, where x_0 is the shelf-break. Thus, we let $x_0 \to \infty$ in (3.4e) [and then also $h_0 \to \infty$, see (3.3b)] and get

$$\frac{\phi_2(x;k)}{W(k)}=-\frac{1}{(k^2+\frac{1}{4}s^2)^{1/2}}\times\exp\left[-\left(k^2+\tfrac{1}{4}s^2\right)^{1/2}x\right], \tag{3.6}$$

while $\phi_1(x;k)$ is unchanged from (3.4c). Substituting the resulting approximation for $\hat{G}$ in (3.1) it can be shown that

$$G(x',x;y'-y)=-\frac{\{h(x')h(x)\}^{1/2}}{2\pi}\left\{K_0\left(\tfrac{1}{2}sR\right)-K_0\left(\tfrac{1}{2}sR_I\right)\right\} \tag{3.7}$$

where R, R_I are defined by (2.18b, c). In obtaining this result we note that (e.g., Magnus and Oberhettinger 1949)

$$K_0[(x^2+y^2)^{1/2}]=\frac{1}{2}\int_{-\infty}^{\infty}\exp(-(k^2+1)^{1/2}|x|+iky)\frac{dk}{(k^2+1)^{1/2}} \tag{3.8}$$

where $K_0(\cdot)$ is the modified Bessel function of the second kind. For future reference we note that as $R \to 0$,

$$K_0(\tfrac{1}{2}sR)=-\ln R-(\gamma+\ln(\tfrac{1}{4}s))+O(R^2\ln R, R^2) \tag{3.9}$$

where γ is Euler's constant. In particular, it follows that in the limit $s \to 0$ (3.7) reduces to (2.18a) as expected.

To simplify notation, we define

$$H(R)\equiv-\frac{1}{2\pi}K_0\left(\frac{1}{2}sR\right). \tag{3.10}$$

Then, substituting the expression (3.7) for G into (2.19a), we get

$$u(x,y)=-\frac{\Delta Q}{\{h(x)\}^{1/2}}\times\int_{-\infty}^{\infty}\{h(L')\}^{3/2}\{H(R')-H(R_I')dL', \tag{3.11a}$$

where

$$R'=\{(x-L')^2+(y-y')^2\}^{1/2}, \tag{3.11b}$$

and

$$R_I'=\{(x+L')^2+(y-y')^2\}^{1/2}. \tag{3.11c}$$

Next we substitute the expression (3.7) for G into (2.17b), and integrate by parts, noting that the terms involving R', R_I' are functions of $(x-x')$ and $(x+x')$ respectively. Hence,

$$v(x,y)-v_0(x)=-\frac{\Delta Q}{\{h(x)\}^{1/2}}\int_{-\infty}^{\infty}\{h(L')\}^{3/2}\{H(R')+H(R_I')\}dy'+\frac{\Delta Q}{\{h(x)\}^{1/2}}\int_{-\infty}^{\infty}h_1^{3/2}\{H(R_0')+H(R_{I0}')\}dy'+\frac{s\Delta Q}{\{h(x)\}^{1/2}}\int_{-\infty}^{\infty}dy'\int_{l}^{L'}\{h(x')\}^{3/2}\times\{2H(R)+H(R_I)\}dx', \tag{3.12a}$$

where

$$R_0'=\{(x-l)^2+(y-y')^2\}^{1/2}, \tag{3.12b}$$

and

$$R_{I0}'=\{(x+l)^2+(y-y')^2\}^{1/2}. \tag{3.12c}$$

Here we recall that R, R_I are defined by (2.18b, c), and note that R_0', R_{I0}' are just R', R_I' with $x'=l$. We see that use of the approximate Green's function (3.7) has enabled us to reduce the expression for $v-v_0$ to three terms, two of which are integrals along the contour $\mathcal{C}$, while the third term remains as an integral over the area occupied by the displaced contour. However,

we expect the main contributions to $v - v_0$ to come from the first two terms, provided that the contour is not displaced too much from its original location (i.e., $x = l$), since the variation in the depth over the region where the contour moves will then be quite small; it is the third term that largely describes this effect. The expressions (3.11a–c) and (3.12a–c) are equivalent to those used by Send (1989) although there are some differences, the most notable being that Send does further differentiations on (3.11a–c) and (3.12a–c) to replace the area integral in (3.12a) by other contour integrals. However, the price paid for this is a higher order of singularity in the extra integrals; we have preferred to leave the area integral in place. Also, Send uses a different formulation of the basic flow, which he includes partly in the perturbation field, with the consequence that the second integral term in (3.12a) is absent. Further, Send treats the boundary condition at $x = 0$ with image contours, whereas we have included the image terms directly in the Green's function; this is preferred because, due to the topographic slope, there is no exact symmetry or antisymmetry, about $x = 0$. We conclude this subsection by noting that the second term in (3.12a) can be evaluated analytically. Indeed

$$\int_{-\infty}^{\infty} \{H(R_0') + H(R_{I0}')\}\, dy' = -\frac{1}{s}\left\{\exp\left(-\tfrac{1}{2}s|x-l|\right) + \exp\left(-\tfrac{1}{2}s|x+l|\right)\right\}. \tag{3.13}$$

To establish this, we note that

$$\frac{1}{2\pi}\int_{-\infty}^{\infty} K_0[(x^2+y^2)^{1/2}]\, dy = \tfrac{1}{2}\exp(-|x|), \tag{3.14}$$

a result which is readily established by taking the inverse Fourier transform of (3.8). Also, on using (3.3a) in (2.10), we get

$$v_0(x) = \Delta Q h_1\left\{-H(l-x)\left[\frac{1}{s}\{1-\exp(-s[l-x])\}\right] + \gamma_1\left[(l-x) - \frac{\delta}{s}\{1-\exp[-s(l-x)]\}\right]\right\} \tag{3.15}$$

where γ_1, δ are defined in (2.22c), while the linear long-wave speed c_0 (2.22b), is here given by

$$c_0 = \frac{1}{s}[1 - \exp(-sl)]. \tag{3.16}$$

b. Numerical method

With the expressions (3.11a) and (3.12a) for u and v, Eqs. (2.8) are integro–differential equations for the evolution of the contour $\mathscr{C}$. The essence of the method of contour dynamics is to represent the contour by N points $(L_i(t), y_i(t))$ for $i = 1, \cdots, N$ in a discretized formulation, so that (2.8) becomes

$$\frac{dL_i}{dt} = u(L_i, y_i), \quad \frac{dy_i}{dt} = v(L_i, y_i), \tag{3.17}$$

where u, v are given by appropriate discretized versions of (3.11a) and (3.12a), respectively. Here, we follow Pratt and Stern (1986) for the numerical approximation of (3.11a) and (3.12a) and use a trapezoidal rule. Thus, (3.11a) is approximated by

$$u(L_i, y_i) = -\frac{\Delta Q}{h_i^{1/2}}\sum_{j=1}^{N+1}{}' \frac{1}{2}(L_j - L_{j-1}) \times \{h_j^{3/2}H(R_{ij}') + h_{j-1}^{3/2}H(R_{ij-1}')\} + \frac{\Delta Q}{h_i^{1/2}} \times \sum_{j=1}^{N+1}\frac{1}{2}(L_j - L_{j-1})\{h_j^{3/2}H(R_{Iij}') + h_{j-1}^{3/2}H(R_{Iij-1}')\} - \Delta Q h_i \int_{L_{i-1}}^{L_{i+1}} \left\{\frac{h(L')}{h_i}\right\}^{3/2} H(R')\, dL', \tag{3.18a}$$

where

$$R_{ij}' = \{(L_i - L_j)^2 + (y_i - y_j)^2\}^{1/2}, \tag{3.18b}$$

$$R_{Iij}' = \{(L_i + L_j)^2 + (y_i - y_j)^2\}^{1/2}, \tag{3.18c}$$

and

$$h_i = h(L_i). \tag{3.18d}$$

Here Σ' denotes the sum over j with the terms $j = i$, $i + 1$ omitted; for notational convenience we introduce the fixed end-points (L_0, y_0) and (L_{n+1}, y_{N+1}), where $L_0 = L_{N+1} = l$, and it is assumed that the contour is not displaced for $y \geq y_0$ and $y \leq y_{N+1}$. The last term in (3.18a) is a singular integral and is evaluated by approximating the curve between (L_{i-1}, y_{i-1}) and (L_{i+1}, y_{i+1}) by a parabola, and then extracting the singular part (cf. Jacobs and Pullin 1989). Thus this part of the contour is represented by

$$L' = L_i + \tfrac{1}{2}(L_{i+1} - L_{i-1})e + \tfrac{1}{2}(L_{i+1} + L_{i-1} - 2L_i)e^2, \tag{3.19a}$$

$$y' = y_i + \tfrac{1}{2}(y_{i+1} - y_{i-1})e + \tfrac{1}{2}(y_{i+1} + y_{i-1} - 2y_i)e^2, \tag{3.19b}$$

where $-1 \leq e \leq 1$ and $e = -1$, 0, 1 correspond to $i - 1, i, i + 1$, respectively. Now we write, recalling (3.3a) for $h(x)$,

$$\int_{L_{i-1}}^{L_{i+1}} \left\{\frac{h(L')}{h_i}\right\}^{3/2} H(R')dL'$$
$$= \int_{-1}^{1} \frac{dL}{de} \exp\left\{\frac{3s}{2}(L' - L_i)\right\} H(R')de$$
$$= -2\alpha + \int_{-1}^{1} \left[\frac{dL'}{de} \exp\left\{\frac{3s}{2}(L' - L_i)\right\} \times H(R') - \alpha \ln|e|\right] de, \quad (3.20a)$$

where

$$2\pi\alpha = \left(\frac{dL'}{de}\right)_{e=0} = \frac{1}{2}(L_{i+1} - L_{i-1}). \quad (3.20b)$$

Here we have used (3.9) to extract the logarithmic singularity from $H(R)$, and evaluated this integral analytically. The remaining integral is evaluated by Simpson's rule.

The approximation for v (3.12a) is similar, but complicated by the necessity to evaluate the tail terms (i.e., the integrals from $-\infty$ to y_0 and from y_{N+1} to ∞), and the area integral (the last term in (3.12a). Hence,

$$v(L_i, y_i) - v_0(L_i) = -\frac{\Delta Q}{h_i^{1/2}} \sum_{j=1}^{N+1}{}' \frac{1}{2}(y_j - y_{j-1})$$
$$\times \{h_j^{3/2} H(R'_{ij}) + h_{j-1}^{3/2} H(R'_{ij-1})\} - \frac{\Delta Q}{h_i^{1/2}}$$
$$\times \sum_{j=1}^{N+1} \frac{1}{2}(y_j - y_{j-1})\{h_j^{3/2} H(R'_{Iij}) + h_{j-1}^{3/2} H(R'_{Iij-1})\}$$
$$- \Delta Q h_i \int_{y_{i-1}}^{y_{i+1}} \left\{\frac{h(L')}{h_i}\right\}^{3/2} H(R')dy' - \frac{\Delta Q h_l^{3/2}}{h_i^{1/2}}$$
$$\times \left\{\int_{-\infty}^{y_0} + \int_{y_{N+1}}^{\infty} [H(R'_i) + H(R'_{Ii})]\right\} dy'$$
$$- \frac{\Delta Q h_1^{3/2}}{s h_i^{1/2}} \left\{\exp\left(-\frac{1}{2}s|L_i - l|\right)\right.$$
$$\left. + \exp\left(-\frac{1}{2}s|L_i + l|\right)\right\} + s\Delta Q h_i$$
$$\times \{\sum_{j=1}^{N} (y_j - y_{j-1})\{2\overline{K_{ij}} + \overline{K_{Iij}}\}\}, \quad (3.21a)$$

where

$$\overline{K_{ij}} = \frac{1}{2}(K_{ij} + K_{ij-1}), \quad \overline{K_{Iij}} = \frac{1}{2}(K_{Iij} + K_{Iij-1}), \quad (3.21b)$$

$$K_{ij} = \int_l^{L_j} \left\{\frac{h(x')}{h_i}\right\}^{3/2} H(R_{ij})dx', \quad (3.21c)$$

and

$$K_{Iij} = \int_l^{L_j} \left\{\frac{h(x')}{h_i}\right\}^{3/2} H(R_{Iij})dx'. \quad (3.21d)$$

Here R'_i, R'_{Ii} are defined by (3.11b, c), respectively, with $x = L_i$, $x' = l$ and $y = y_i$, while R_{ij}, R_{Iij} are defined by (2.18b, c), respectively, with $x = L_i$, $y = y_i$ and $y' = y_j$. The second integral term in (3.12a) has been evaluated analytically using (3.13). The singular integral in the third term in (3.21a) is evaluated in an analogous manner to (3.20a), hence

$$\int_{y_{i-1}}^{y_{i+1}} \left\{\frac{h(L')}{h_i}\right\}^{3/2} H(R')dy' = -2\beta$$
$$+ \int_{-1}^{1} \left[\frac{dy'}{de} \exp\left\{\frac{3s}{2}(L' - L_i)\right\} H(R') - \beta \ln|e|\right] de, \quad (3.22a)$$

where

$$2\pi\beta = \left(\frac{dy'}{de}\right)_{e=0} = \frac{1}{2}(y_{i+1} - y_{i-1}). \quad (3.22b)$$

The tail integrals in the fourth term of (3.21a) are evaluated by Simpson's rule over the ranges $P + y_0 \leqslant y' \leqslant y_0$ or $y_{N+1} \leqslant y' \leqslant y_{N+1} + P$ where P is chosen large enough for the Bessel function integrands to achieve exponential smallness. The new feature here is the presence of the integral terms K_{ij}, K_{Iij} which are also evaluated by Simpson's rule. However, K_{ii} has a singularity at $x' = L_i$ and is evaluated by first extracting the singularity as follows:

$$K_{ii} = \frac{1}{2\pi}(L_i - l)\{\ln(|L_i - l|) - 1\}$$
$$+ \int_0^{L_i - l} \left\{\exp\left(-\frac{3}{2}s\xi\right) H(|\xi|) - \frac{1}{2\pi}\ln(|\xi|)\right\} d\xi, \quad (3.23)$$

where the integral is again evaluated by Simpson's rule.

The ordinary differential equations (3.17) are stepped forward in time using a standard fourth-order Runge–Kutta method. As time progresses the nodal points tend to clump together in some places and to diverge in other places. Hence it is necessary to use a node insertion/deletion scheme to maintain adequate resolution. The scheme used here is based on that described by Pullin and Jacobs (1986). Briefly, a node is inserted between the points (L_i, y_i) and (L_{i+1}, y_{i+1}) if

$$\Delta_i = \{(L_{i+1} - L_i)^2 + (y_{i+1} - y_i)^2\}^{1/2} > \epsilon, \quad (3.24a)$$

where

$$\epsilon = \max\left[\min\left(\frac{1}{2}d_{\min}, \frac{1}{6\kappa}, S_{\max}, 4S_{\text{adj}}\right), 0.2\right], \quad (3.24b)$$

$$d_{\min} = \max[S_{\min}, 0.02], \quad (3.24c)$$

$$S_{\max} = \min[P_{\text{av}}, 0.2], \quad (3.24d)$$

and

$$S_{\text{adj}} = \min[\Delta_{i-1}, \Delta_{i+1}], \quad (3.24e)$$

while κ is the curvature of the local contour segment estimated by fitting a parabola between the ith and $(i+1)$th nodes, $S_{\min}$ is the minimum distance of approach of nonadjacent parts of the contour, and P_{av} is the average length of the current contour segment. A node is deleted if $\Delta_i < \min[\epsilon/10, 0.02]$. The actual numerical values used here were obtained by extensive testing and are suitable for the present application, although for some calculations different values were used depending on the total range of y (i.e., $y_{N+1} - y_0$) and the total number of initial nodes; also not all of the criteria in (3.24b) were always needed, and occasionally some were omitted to improve computational efficiency.

4. Results

Apart from parameters introduced through the initial condition (see below), the available parameters are $\Delta Q h_1$, $\gamma_1 = f/\Delta Q h_1$, $\delta = h_1/h_0$ and s, where the topographic slope is the exponential depth profile $h = h_1 \exp(s(x-l))$ for $0 < x < x_0$, $h = h_0$ for $x > x_0$, $h_1 = h(l)$ and h_0 is the depth of the ocean. Here l is the undisturbed distance of the potential vorticity front from the coast at $x = 0$, and there is no loss of generality in putting $l = 1$. Next it can be shown from (3.11a) and (3.12a) that $|\Delta Q h_1|$ determines the time scale. Further, a change of sign of $\Delta Q h_1$, with all other parameters fixed, simply reverses the direction of the wave evolution (i.e., is equivalent to a change of sign of y). Hence there is no loss of generality in putting $\Delta Q h_1 = -1$. Next, our approximation for the Green's function in section 3a used the limit $h_0 \to \infty$, which requires that $\delta = 0$, although some calculations were nevertheless carried out with $\delta \neq 0$ [in (3.15)]. Thus, the two remaining parameters are the topographic slope s and γ_1. Most of the calculations were carried out with $s = 1$, although we shall report on some calculations for other values of s. The parameter γ_1 is an inverse measure of the strength of the potential vorticity front (i.e., ΔQ) to the background potential vorticity f/h_1. Note that the quasi-geostrophic limit corresponds to $s \to 0$, $\gamma_1 \to \infty$ with the product $\gamma_1 s$ held fixed. In most of the calculations reported here we put $\gamma_1 = 5$ or -5, and note that the choice of sign is significant. Finally, in a typical calculation we begin with about 100 nodal points, and allow this to increase to a maximum of 200 nodal points.

Since our main aim is the study of wave evolution and the comparison with long-wave theories, we at first choose the initial condition

$$L(y, 0) = 1 + a_0 \operatorname{sech}^2 \beta y, \quad (4.1)$$

which introduces two further parameters, the initial wave amplitude a_0 and the initial wavelength, which is measured by β^{-1}. The fixed end points y_0, y_{N+1} are chosen in each calculation to be sufficiently remote from the evolving wave so that the assumption that they remain fixed is valid for as long as possible. As a check on the code we monitored the depth-integrated area of the displaced contour,

$$\mathcal{A} = \int_{-\infty}^{\infty} \left(\int_{l}^{L(y,t)} h(x')dx' \right) dy, \quad (4.2)$$

which is a conserved quantity. This is most readily shown from the kinematic condition (2.7) in the form (2.22). In practice, $\mathcal{A}$ was conserved to three significant figures for the calculations reported here.

Before proceeding to describe our main results, we show in Fig. 2 a typical result for the evolution of a long wave. This is obtained for an initial amplitude $a_0 = 0.1$, and $\beta = 1.0$ in (4.1), with $s = 1$, $\gamma_1 = 5$ and $\delta = 0$. To aid in the comparison with the long-wave calculations of Grimshaw and Yi (1990), the results are shown in the same format of contour plots of A, where $A = L - l$, in the x–t plane. We see that there is a tendency for the wave to steepen, with the formation of a small depression in the lee of the wave. This is in qualitative agreement with the results of Grimshaw and Yi. However, a quantitative comparison is not possible

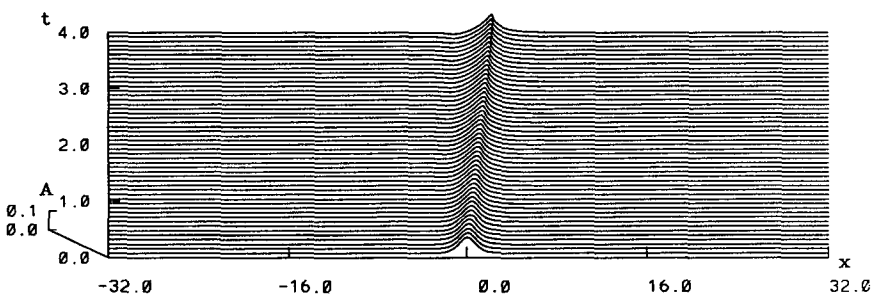

FIG. 2. A typical result for the evolution of a long wave from the initial condition (4.1): $\Delta Q h_1 = -1$, $\gamma_1 = 5$, $\delta = 0$, $s = 1$, $a_0 = 0.1$, $\beta = 1$.

because of the different choices for the depth profile and the different treatment there of the shelf-break condition (see the discussion here in the last paragraph of section 2 for a summary of the approach used in Grimshaw and Yi). Instead, the results in Fig. 2 can be compared with the predictions from the weakly nonlinear, nondispersive limit (2.22). The simplest comparison is the linear long-wave speed c_0 (2.23b) [see also (3.16)]. For the case shown in Fig. 2, the observed speed is slightly less than c_0, presumably due to dispersive effects, since decreasing β in (4.1) was found to cause the observed speed to approach c_0.

Next, to study the consequences of wave steepening we show in Fig. 3 the results when $a_0 = 0.1$ or 0.2 and $\beta = 5$ in the initial condition (4.1). The remaining parameters are $s = 1$, $\gamma_1 = 5$, and $\delta = 0$. In both cases the wave initially steepens and breaks forward, in agreement with the predictions of the weakly nonlinear,

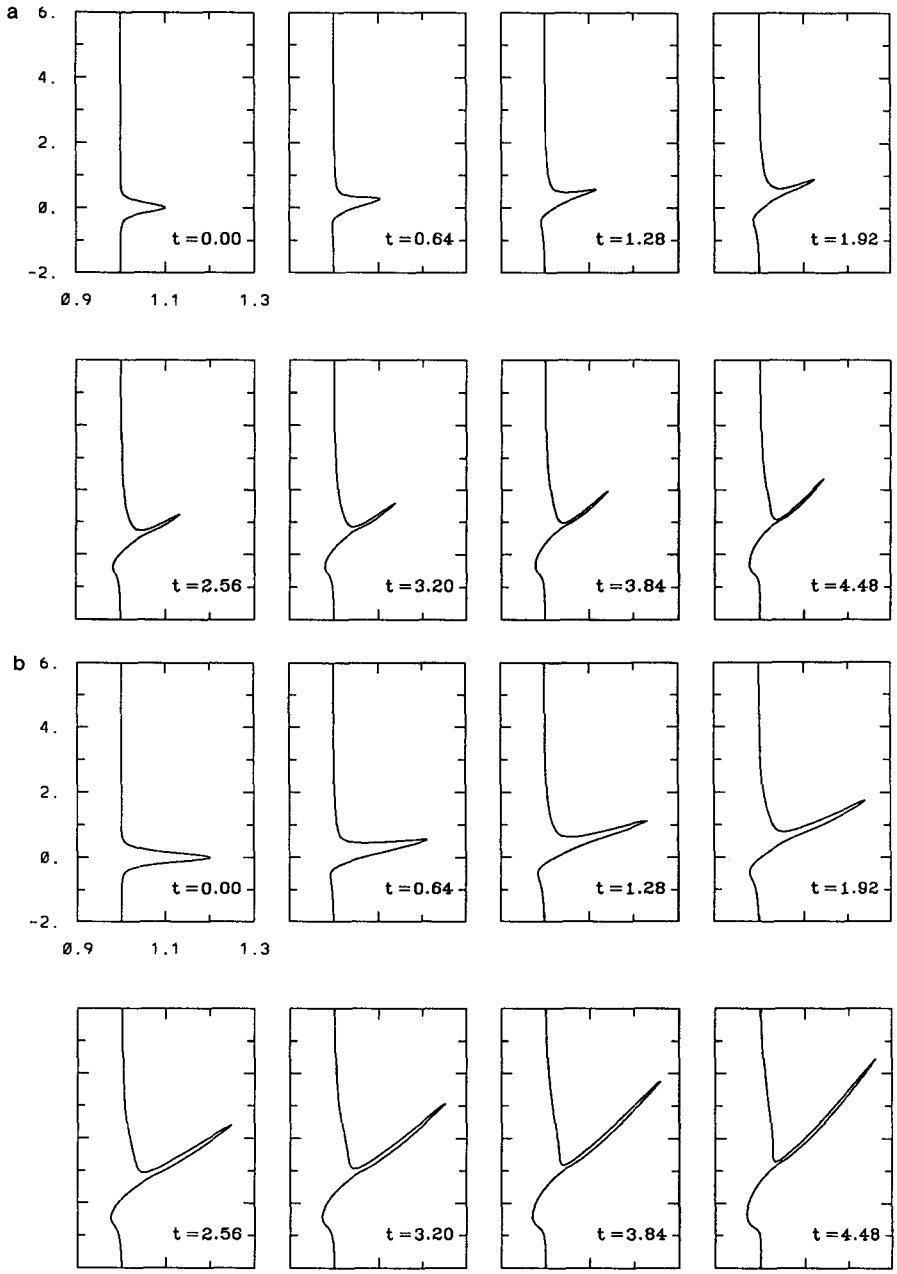

FIG. 3. Typical results for the initial condition (4.1) with $\gamma_1 > 0$ and $a_0 > 0$: $\Delta Q h_1 = -1$, $\gamma_1 = 5$, $\delta = 0$, $s = 1$, $\beta = 5$ and (a) $a_0 = 0.1$, (b) $a_0 = 0.2$. In these and all subsequent plots the x and y axes are the horizontal and vertical axes, respectively.

nondispersive equation (2.23). However, as time progresses the breaking wave evolves into a thin filament while a depression forms and deepens behind the filament. Also noteworthy is the gradual rise of the interface in the region ahead of the filament. Increasing the initial amplitude from $a_0 = 0.1$ to $a_0 = 0.2$ did not cause any qualitative changes. We also found that varying s in the range 0.5 to 2, or putting $\delta = 0.2$, did not change the qualitative picture or introduce significant quantitative changes. Increasing the slope s beyond 2 did cause some changes which are reported later (see Fig. 7).

In Fig. 4, we set $a_0 = 0.1$ or 0.2, $\beta = 5$ in the initial condition (4.1), again put $s = 1$, $\delta = 0$, but now put $\gamma_1 = -5$. This corresponds to changing the sign of f. The evolution is now quite different. The initial tendency is for the wave to propagate in the negative y-direction, even though the linear long-wave speed is positive. This indicates that even with $a_0 = 0.1$, the nonlinear effects are significant. At the same time a

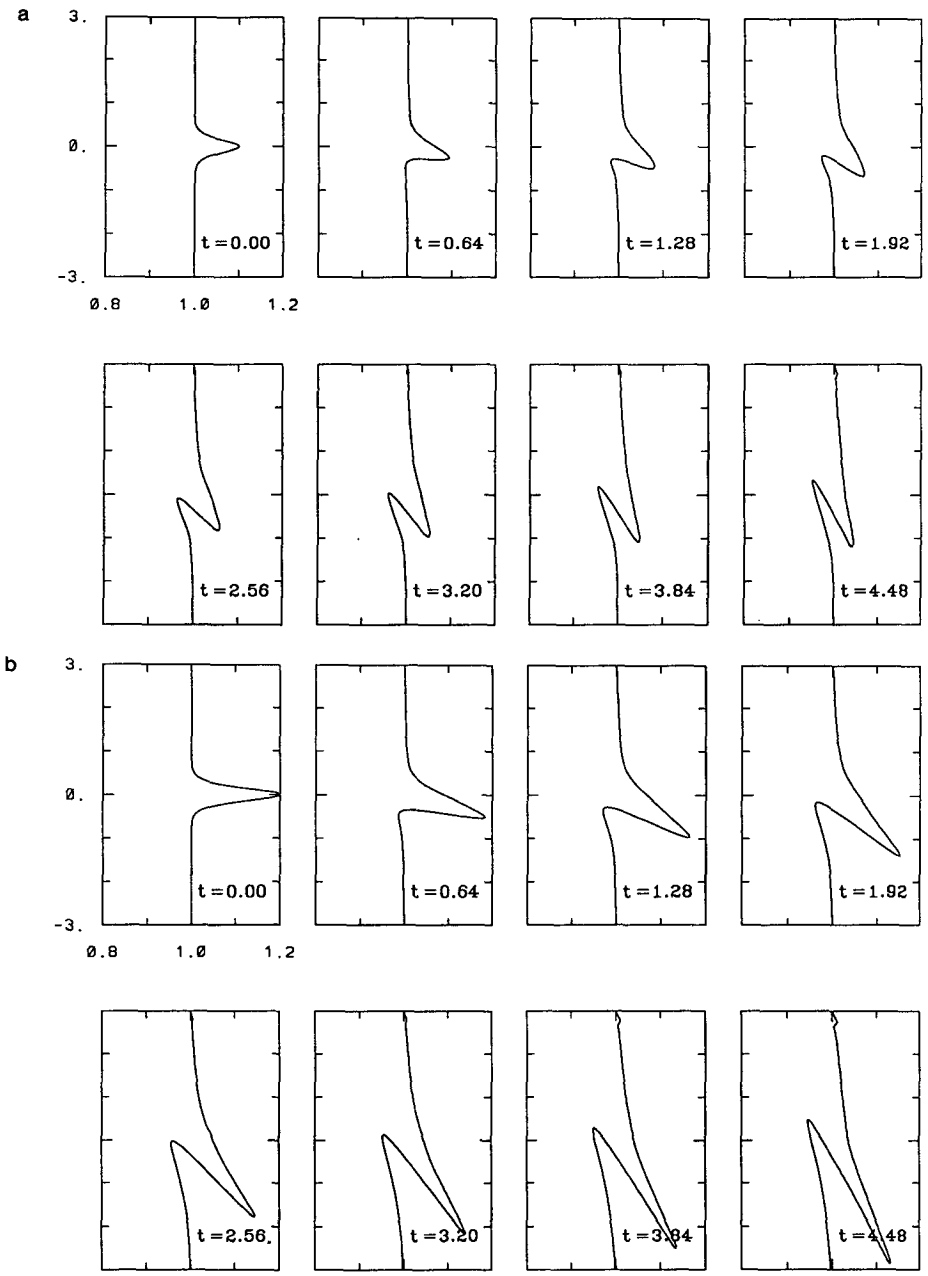

FIG. 4. As in Fig. 3 but with $\gamma_1 < 0$ and $a_0 > 0$: $\Delta Q h_1 = -1$, $\gamma_1 = -5$, $\delta = 0$, $s = 1$, $\beta = 5$ and (a) $a_0 = 0.1$, (b) $a_0 = 0.2$.

depression develops, and propagates in the positive y-direction. Presumably this skewing of the wave will eventually result in the formation of two filaments.

In Fig. 5a we consider the consequences of putting $\gamma_1 = 0.2$, with the remaining parameters unchanged from Fig. 4. This corresponds to increasing the strength of the front vis-a-vis the background. There is now little tendency for the wave to propagate, although some movement in the negative y-direction can be detected. Instead, a depression develops in the lee (now on the positive side given the slight movement in the negative direction), and appears to deepen without much sign of propagation. The contrast with the results in Fig. 3 is obvious, and the changeover between the two types of behavior as γ_1 is decreased through positive values occurs at about $\gamma_1 = 1.7$ [see Fig. 5(b)].

In Fig. 6, we show two cases with $a_0 = -0.2$, $\gamma_1 = 5$ or -5, and the remaining parameters unchanged from Fig. 3. There is a clear resemblance between the case $a_0 < 0$ and $\gamma_1 > 0 (<0)$ with the corresponding cases

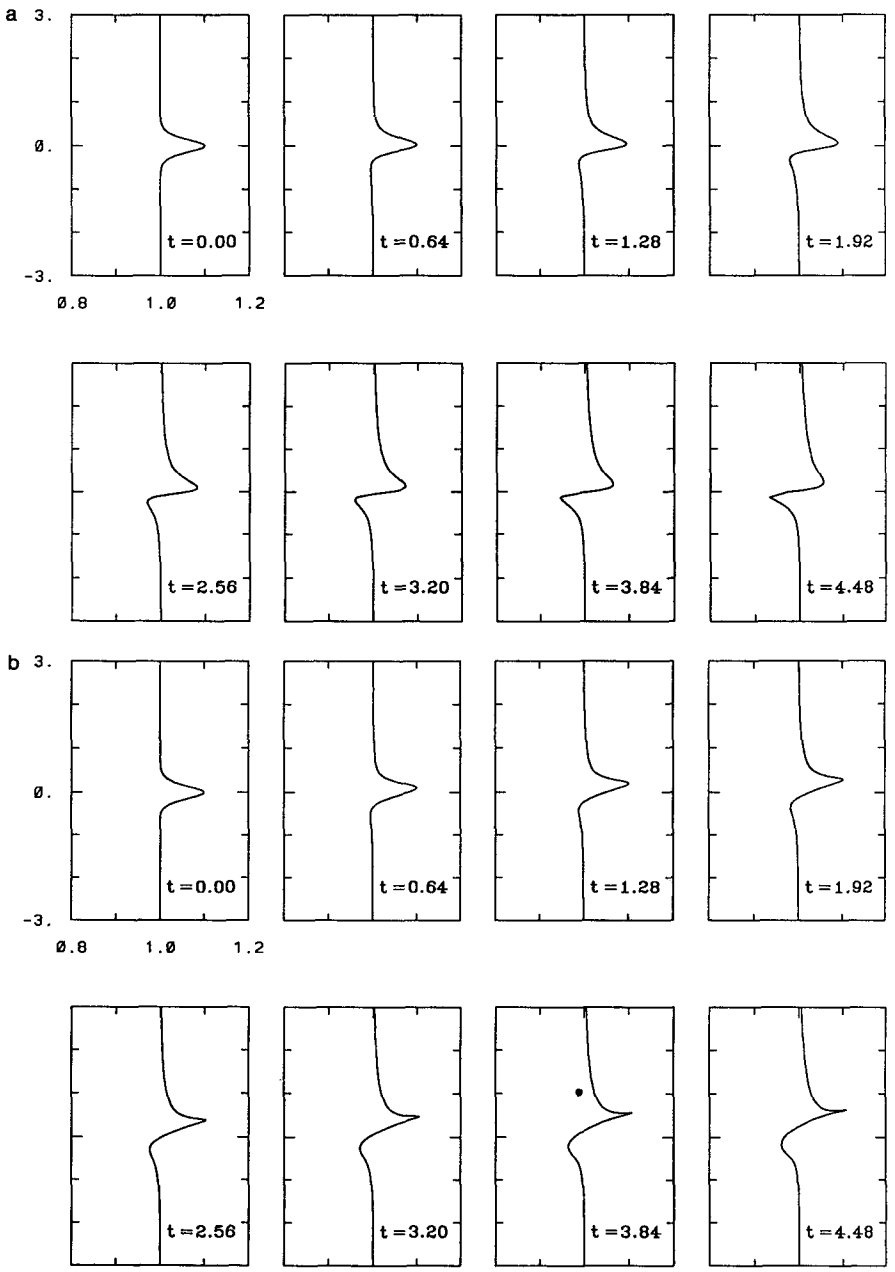

FIG. 5. As in Fig. 3 but as γ_1 is varied. Here $\Delta Qh_1 = -1$, $\delta = 0$, $s = 1$, $a_0 = 0.1$, $\beta = 5$ and (a) $\gamma_1 = 0.2$, (b) $\gamma_1 = 1.7$.

$a_0 > 0$ and $\gamma_1 < 0 (>0)$ [see Figs. 4b and 3b respectively], which extends even to approximate quantitative agreement when $a_0 = -0.1$. This antisymmetry is to be expected in the absence of a topographic slope (i.e., $s = 0$) and for the absence of a coast at $x = 0$. However, even for an amplitude $a_0 = -0.2$ as small as that shown in Fig. 6, there are some observable effects of the slope and coast. For $a_0\gamma_1 > 0$, comparing Figs. 3b and 6b we see that, with the initial displacement towards the coast and into the shallower water, there is an enhanced tendency for filament formation and the wave speed increases. However, for $a_0\gamma_1 < 0$, this tendency is reversed. A simple explanation of these tendencies can be found by examining the expression (3.15) for $v_0(x)$. Recalling that $v_0(l) = 0$, we see from (3.15) that the basic current shear v_{0x} is $-\Delta Q h_1 \gamma_1$ as $x \to l+$ and $-\Delta Q h_1(\gamma_1 - 1)$ as $x \to l-$. Since $\Delta Q h_1 < 0$ was chosen, this implies that for $\gamma_1 > 0$ there is a

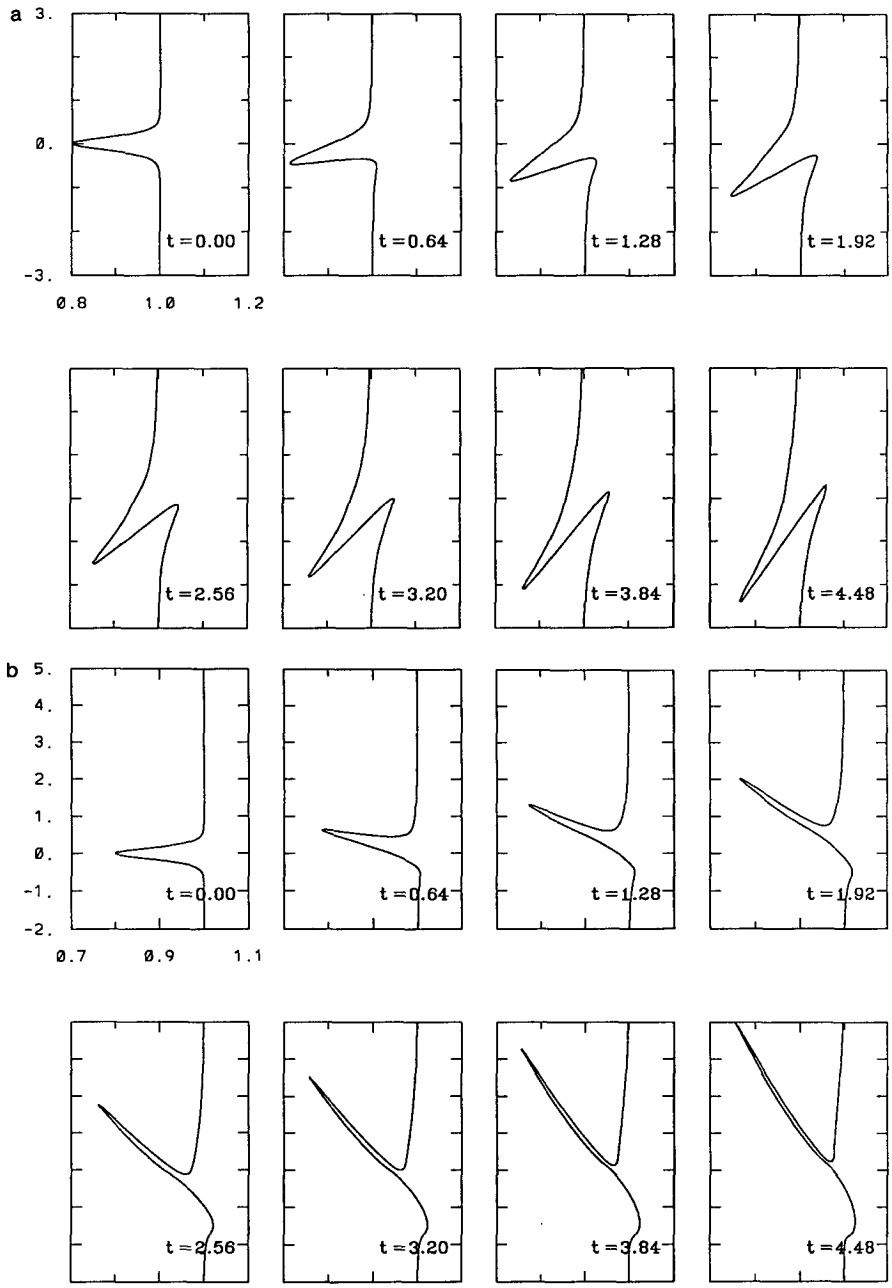

FIG. 6. Typical results for the initial condition (4.1) with $a_0 < 0$: $\Delta Q h_1 = -1$, $\delta = 0$, $s = 1$, $a_0 = -0.2$, $\beta = 5$ and (a) $\gamma_1 = 5$, (b) $\gamma_1 = -5$.

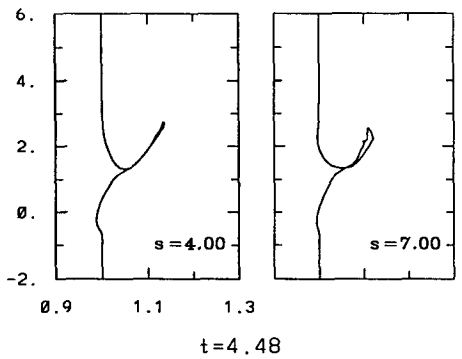

FIG. 7. Typical results for the initial condition (4.1) as the topographic slope s is varied: $\Delta Qh_1 = -1$, $\gamma_1 = 5$, $\delta = 0$, $a_0 = 0.1$, $\beta = 5$ and (a) $s = 4$, (b) $s = 7$. Only the results for $t = 4.48$ are shown.

relatively stronger magnitude for the positive current in $x > l$ than there is for the negative current in $x < l$ (see Fig. 1). The situation is reversed for $\gamma_1 < 0$.

In Fig. 7, we show the effect of increasing the topographic slope to $s = 4$ or 7, for the same initial condition shown in Fig. 3a. Interestingly, these steeper topographic slopes result in enhanced filamentation and a tendency for the tip of the filament to develop into a detached eddy.

All results shown so far are for the initial condition (4.1) with $|a_0| = 0.1$ or 0.2, which represents a small-amplitude wave. With the exception of the last result shown in Fig. 7, no tendency was found for the wave to evolve into a detached eddy. This is in agreement with the results of Pratt and Stern (1986), who conclude that "fairly extreme initial conditions" are needed to get eddy detachment. Indeed, we find that retaining the smooth shape of (4.1) but increasing $|a_0|$ does not lead to any significant tendency for eddy detachment, although it is of course conceivable that the thin filaments formed, for example, in Fig. 3b, might eventually wrap around to form an eddy. However, our present capacity for numerical resolution prevents us from pursuing this possibility. Instead, we follow the procedure of Pratt and Stern (1986) and replace the initial condition (4.1) with

$$L(y, 0) = 1 + \tfrac{1}{2} a_1 \{1 \mp \tanh[s_0(y \mp w)]\}, \quad \text{for} \quad y \gtrless 0, \quad (4.3)$$

which for large values of s_0 describes an approximation to a square wave with amplitude a_1. Then sufficiently narrow waves of large amplitude will evolve to a point where eddy detachment is about to occur. Of course, our contour dynamics algorithm does not allow for contour surgery, so we are unable to see the eddy actually form. A typical result is shown in Fig. 8 for $a_1 = 3.6$, $s_0 = 10$ and $w = 1.5$. This large-amplitude wave requires much greater resolution, so we commence with nearly 400 nodal points and allow this to increase to nearly 600 nodal points. Now an eddy begins to form at the tip of the wave, although the evolving wave also contains other features such as filament formation. The overall picture is similar to the results of Pratt and Stern (1986) although there are some significant differences, notably the thin filament propagating towards the coast in the negative y-direction at the front of the

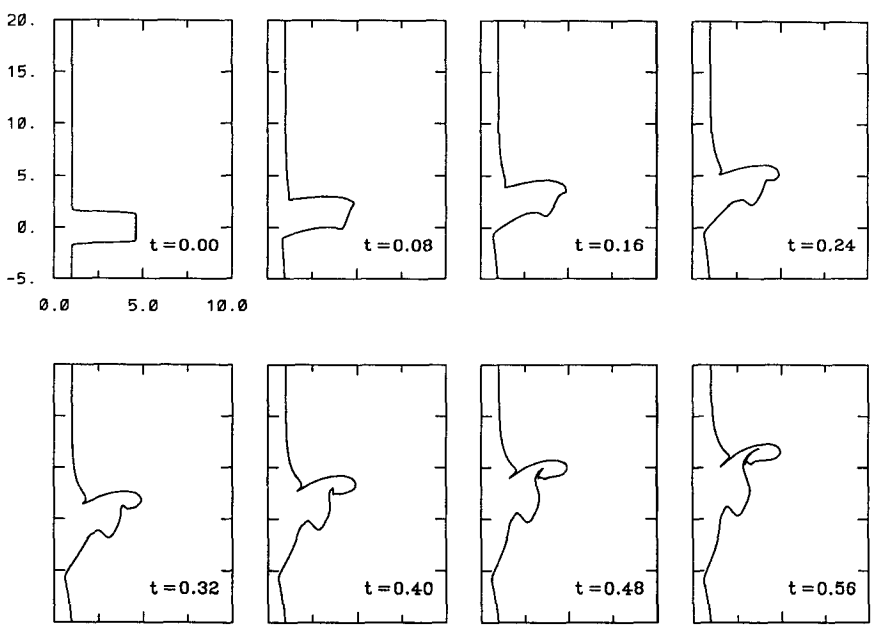

FIG. 8. A typical result for the evolution of a large-amplitude square wave. The initial condition is (4.3) with $a_1 = 3.6$, $s_0 = 10$, and $w = 1.5$ Here $\Delta Qh_1 = -1$, $\delta = 0$, $s = 1$, and $\gamma_1 = 5$.

wave. The result shown in Fig. 8 is robust in that varying the number of nodal points, or modifying the node insertion/deletion scheme, did not change the result in any significant way. It is appropriate to note here that the main difference between the present model and that used by Pratt and Stern (1986) is that the latter in essence replaces (2.13a) for the streamfunction anomaly with a Helmholtz equation on the left-hand side and a piecewise constant function on the right-hand side [i.e., there are no inhomogeneous terms such as those due to $h(x)$ in (2.13a)]. Thus, their model contains a finite deformation radius, and this seems to provide a length scale for eddies to form. However, although our equation (2.13a) is closer in form to Poisson's equation, an examination of our Green's function (3.7) shows that there is an effective deformation radius of s^{-1}, the inverse of the topographic slope. Hence it is not surprising that our large-amplitude studies are generally similar to Pratt and Stern (1986).

5. Discussion

The main aim of this study has been to determine the evolution of small-amplitude waves on a potential vorticity front. These results are summarized in Figs. 3 to 7. In each case the wave at first deforms according to the predictions of the weakly nonlinear, nondispersive equation (2.23a). It is significant here that our choice of values for the parameters s, γ_1 and δ generally implies that the nonlinear steepening term in (2.23a) dominates the linear term which describes propagation at speed c_0. In our previous theory (Grimshaw and Yi 1990) weak dispersion was invoked to balance the steepening process. However, in that theory the dispersive terms were associated with shelf-break processes, which are absent in the present study because we have used the approximation $h_0 \gg h_1$. Hence, we find here that wave steepening generally leads to filament formation, although there is sufficient dispersion associated with the topographic slope alone to produce a significant depression behind the wave (see, for instance, Figs. 3a,b). In some instances this depression deepens and begins to form a filament, becoming itself a major feature (see, for instance, Figs. 4a,b and 5a). Further, it is useful to note that although the weakly nonlinear, nondispersive equation (2.23a) provides the best guide to the initial movement of the wave, simple advection by the basic flow $v_0(x)$ (3.15) also gives a crude guide to the initial wave evolution. Note that $v_0(l) = 0$ and the basic current shear v_{0x} is $-\Delta Q h_1 \gamma_1$ as $x \to l+$ and $-\Delta Q h_1(\gamma_1 - 1)$ as $x \to l-$ (see Fig. 1). With $\Delta Q h_1 < 0$ this leads to forward (backward) steepening for $a_0\gamma_1 > 0 (<0)$.

Next we turn to the filamentation process itself. First we note that conservation of the depth-integrated area of (4.2) leads to a gradual rise (i.e., a displacement in the same sense as the initial wave) ahead of the main wave. The front of this rise propagates in the positive y-direction at the linear long-wave speed c_0. When this front reaches $y = y_{N+1}$ errors are introduced into the computation since our algorithm requires the point (L_{N+1}, y_{N+1}) to be fixed with $L_{N+1} = l$. However, these errors, particularly noticeable for instance in Fig. 4b, remain localized, and do not affect significantly the filament behavior. That filamentation occurs here as a consequence of wave evolution is not surprising, as contour dynamics simulations in a variety of contexts have demonstrated that filamentation is an ubiquitous feature of the unsteady evolution of vorticity fronts (see, for instance, the review by Dritschel 1989). In the present context the process leading to filamentation is generally wave steepening by nonlinear effects where clearly, for the present parameter values, wave dispersion is too weak to prevent filaments forming. In the terminology of Pullin et al. (1990), filamentation occurs by a kinematic mechanism.

To explore this latter concept more fully, we first note that the basic flow $v_0(x)$ (3.15) is linearly stable. Indeed the basic flow $v_0(x)$ given by (2.10) is linearly stable for all depth profiles $h(x)$. Returning to (3.15) it can be shown that infinitesimally small-amplitude waves of wavenumber k have a phase speed c given by

$$c = -\frac{\Delta Q h_1}{2(k^2 + \frac{1}{4}s^2)^{1/2}} \times \left\{1 - \exp\left[\left(k^2 + \frac{1}{4}s^2\right)^{1/2} 2l\right]\right\}, \quad (5.1)$$

where the limit $h_0 \to \infty$ (i.e., $\delta = 0$) has been taken for simplicity. Note that the limit $k \to 0$ gives the linear long-wave speed c_0 (3.16), while otherwise c decreases as either $|k|$ or s increases. Pullin et al. (1990) adapt the suggestion by Pullin (1981) that filamentation will occur when the initial wave contains a dominant Fourier component with wavenumber k which contains a critical layer. They propose that filamentation will occur when a hyperbolic stagnation point (in a suitable frame of reference) almost coincides with an interface extremum. Here, in a frame of reference moving with speed c, a critical layer provides a suitable stagnation point. Strictly, to calculate the position of the critical layer, we should take account of the flow field due to the initial wave [i.e., that given (4.1)], but since our attention is restricted here to small-amplitude waves, we estimate the critical layer position x_c by putting $v_0(x_c) = c$. For instance, with the parameter setting of Fig. 3 (i.e., $l = 1$, $s = 1$, $\Delta Q h_1 = -1$), and putting $k = 1$ as a representative wavenumber for the initial condition (4.1) with $\beta = 5$, we find that $x_c - l \approx 0.08$ for $\gamma_1 = 5$, and -0.067 for $\gamma_1 = -5$. This implies that waves of amplitudes $a_0 > 0.08$ should filament for $\gamma_1 = 5$, but not when $\gamma_1 = -5$. Our results for $\gamma_1 = 5$ support this conjecture (see Figs. 3a,b), and while results for $\gamma_1 = -5$ (see Figs. 4a,b) suggest that the waves are evolving into filaments, the evolution is much less

pronounced than for $\gamma_1 = 5$, and in this sense supports the proposed kinematic mechanism. Further, with $k = 0$, the critical layer position moves to $x_c - l \approx 0.13$ and implies that a long wave of amplitude $a_0 = 0.1$ will not filament, in agreement with our results shown in Fig. 2. Two further tests of the mechanism can be made. First, with $l = 1$, $s = 1$, $\Delta Qh_1 = -1$, and $k = 1$ the critical layer is given by $x_c - l = 0.235$ for $\gamma_1 = 1.7$, and $x_c - l \approx -0.5$ for $\gamma_1 = 0.2$. This implies that a wave of amplitude $a_0 = 0.1$ will filament in the region $x > l$ for $\gamma_1 = 1.7$ but not when $\gamma_1 = 0.2$, in agreement with the results in Fig. 5a,b. Also, we note that with $\gamma_1 = 0.2$, it is the negative depression which starts to show signs of filamentation, in agreement with the fact that the critical layer $x_c < l$. Next, as the slope s increases, the phase speed c (5.1) decreases, thus shifting the critical layer closer to $x = l$. This implies that increasing the slope s will enhance filamentation in agreement with our results shown in Fig. 7. In summary, filamentation is essentially controlled by local nonlinear vorticity dynamics, and the main role of the topographic and potential vorticity parameters (i.e., s, γ_1) is to control the position of the critical level, and hence determine the onset of filamentation. Incidentally, a similar interpretation is possible for the results of Stern and Pratt (1985), who found that small amplitude waves on an evolving undular bore did not filament, in contrast to larger amplitude waves. A quantitative investigation of their results is not possible due to difficulties in estimating an appropriate wavenumber k, but their results are consistent with the observation that as the strength of the bore is increased, thus producing larger waves, the critical level for a given wavenumber k moves relatively closer to the interface defining the undular bore.

We turn next to the interpretation of the present theoretical results in the context of observations of meanders and other pronounced features of coastal currents. Of course, the present model has been adopted for analytical convenience and, in particular, neglects the effects of stratification and friction. Further, we have used a very special basic potential vorticity profile in order to allow the development of a contour dynamics algorithm. However, it is apparent from our results, and from the many other contour dynamic simulations in the literature, that filamentation is an ubiquitous and robust process. We conclude that current meanders and squirts can be due entirely to the kind of nonlinear vorticity dynamics described here and that it is not always necessary to invoke an underlying linear instability (e.g., baroclinic instability) of the basic flow in order to explain the growth of prominent features on coastal currents. Of course, the presence of a linear instability mechanism could well act in concert with filamentation dynamics by promoting initial wave growth to the point where filamentation then occurs. Indeed, Send (1989) has considered wave evolution over a topographic slope for an unstable basic flow, and found that, for small-amplitude initial disturbances, linear instability theory provides the selection mechanism for the alongshore scale and the initial wave growth, which is then following by filamentation. However, he did not discuss the actual filamentation process itself.

Finally we note that for all our small-amplitude simulations there was no tendency for the wave to evolve into a detached eddy. Indeed, in agreement with the results of Pratt and Stern (1986), we find that only large-amplitude waves of narrow aspect can readily evolve to a state where it seems that an eddy is about to form. Even then, however, it seems that eddy detachment is caused by local filamentation of a portion of the interface (see Fig. 8). But to conclude we should comment that if the underlying basic flow were linearly unstable then it is conceivable that a small-amplitude wave could grow to a point where subsequent filamentation would lead to eddy detachment (see Send 1989).

Acknowledgments. One of us (Yi) acknowledges support from ARC Grant A88830746. We also gratefully thank Dr. D. I. Pullin for his advice during the development of this work.

REFERENCES

Dritschel, D. G., 1989: Contour dynamics and contour surgery: numerical algorithms for extended, high-resolution modeling of vortex dynamics in two-dimensional, inviscid, incompressible flows. *Comput. Phys. Rep.*, **10,** 77–146.

Grimshaw R., and Z. Yi, 1990: Finite-amplitude long waves on coastal currents. *J. Phys. Oceanogr.*, **20,** 3–18.

Jacobs, P. A., and D. I. Pullin, 1989: Multiple-contour-dynamic simulation of eddy scales in the plane shear layer. *J. Fluid Mech.*, **199,** 89–124.

Magnus, W., and F. Oberhettinger, 1949: *Formulas and Theorems for the Special Functions of Mathematical Physics.* Chelsea, 172 pp.

Pratt, L. J., and M. E. Stern, 1986: Dynamics of potential vorticity fronts and eddy detachment. *J. Phys. Oceanogr.*, **16,** 1101–1120.

Pullin, D. I., 1981: The nonlinear behaviour of a constant vorticity layer at a wall. *J. Fluid Mech.*, **108,** 401–421.

——, and P. A. Jacobs, 1986: Inviscid evolution of stretched vortex arrays. *J. Fluid Mech.*, **171,** 377–406.

——, ——, R. H. J. Grimshaw and P. G. Saffman, 1990: Instability and filamentation of finite-amplitude waves on vortex layers of finite thickness. *J. Fluid Mech.*, **209,** 359–384.

Send, U., 1989: Vorticity and instability during flow reversals on the continental shelf. *J. Phys. Oceanogr.*, **19,** 1620–1633.

Stern, M. E., and L. J. Pratt, 1985: Dynamics of vorticity fronts. *J. Fluid Mech.*, **161,** 513–532.